



HAL
open science

The ALPINE-ALMA [CII] survey: The population of [CII]-undetected galaxies and their role in the L[CII]-SFR relation

M. Romano, L. Morselli, P. Cassata, M. Ginolfi, D. Schaerer, M. Béthermin, P. Capak, A. Faisst, O. Le Fèvre, J. D. Silverman, et al.

► **To cite this version:**

M. Romano, L. Morselli, P. Cassata, M. Ginolfi, D. Schaerer, et al.. The ALPINE-ALMA [CII] survey: The population of [CII]-undetected galaxies and their role in the L[CII]-SFR relation. *Astronomy and Astrophysics - A&A*, 2022, 660, 10.1051/0004-6361/202142265 . insu-03667445

HAL Id: insu-03667445

<https://insu.hal.science/insu-03667445>

Submitted on 14 May 2022

HAL is a multi-disciplinary open access archive for the deposit and dissemination of scientific research documents, whether they are published or not. The documents may come from teaching and research institutions in France or abroad, or from public or private research centers.

L'archive ouverte pluridisciplinaire **HAL**, est destinée au dépôt et à la diffusion de documents scientifiques de niveau recherche, publiés ou non, émanant des établissements d'enseignement et de recherche français ou étrangers, des laboratoires publics ou privés.

The ALPINE-ALMA [CII] survey: The population of [CII]-undetected galaxies and their role in the $L_{\text{[CII]}}$ -SFR relation

M. Romano^{1,2,3} , L. Morselli⁴, P. Cassata^{1,2}, M. Ginolfi⁵, D. Schaerer⁶, M. Béthermin⁷, P. Capak⁸, A. Faisst⁹, O. Le Fèvre^{7,†}, J. D. Silverman^{10,11}, L. Yan¹², S. Bardelli¹³, M. Boquien¹⁴, M. Dessauges-Zavadsky⁶, S. Fujimoto^{15,16}, N. P. Hathi¹⁷, G. C. Jones^{18,19}, A. M. Koekemoer¹⁷, B. C. Lemaux^{20,21}, H. Méndez-Hernández²², D. Narayanan^{23,24,25}, M. Talia^{26,13}, D. Vergani¹³, G. Zamorani¹³, and E. Zucca¹³

(Affiliations can be found after the references)

Received 20 September 2021 / Accepted 4 February 2022

ABSTRACT

The [CII] 158 μm emission line represents one of the most profitable tools for the investigation of the high-redshift galaxies in the early Universe so far. Being one of the brightest cooling lines in the rest-frame far-infrared regime of star-forming galaxies, it has been successfully exploited as a tracer of the star-formation rate (SFR) in local sources. The picture is more complex at higher redshifts, where its usability in this context is still under investigation. Recent results from the ALMA Large Program to INvestigate [CII] at Early times (ALPINE) survey suggest that there is no (or weak) evolution of the $L_{\text{[CII]}}$ -SFR relation up to $z \sim 6$, but their reliability is hampered by the presence of a large population of [CII] nondetected galaxies. In this work, we characterize the population of [CII] nondetections in ALPINE. By stacking their ALMA spectra, we obtained a signal detected at $\sim 5.1\sigma$, resulting in a [CII] luminosity of $\log(L_{\text{[CII]}}/L_{\odot}) \sim 7.8$. When combining this value with those from the [CII] detections, we found a $L_{\text{[CII]}}$ -SFR relation with a slope $b = 1.14 \pm 0.11$, which is in agreement within the uncertainties both with the linear relation found in the local Universe and with the previous findings from ALPINE at $z \sim 5$. This suggests that the [CII] line can be considered a good tracer of star formation up to the distant Universe. Finally, we show that the galaxies of our sample that deviate from the observed $L_{\text{[CII]}}$ -SFR relation most could suffer from a less precise redshift estimation, perhaps artificially reducing their [CII] luminosity. In this respect, we claim that there is no evidence in favor of a deficit of [CII] content in high- z galaxies, in contrast with earlier studies.

Key words. galaxies: high-redshift – galaxies: evolution – galaxies: formation

1. Introduction

Over the last years, observations of the [CII] line emission at 158 μm rest-frame in galaxies have progressively improved to the point of being able to characterize the first sources of light during or near the epoch of cosmic reionization (e.g., Wagg et al. 2012; Carilli & Walter 2013; Wang et al. 2013; Capak et al. 2015; Pentericci et al. 2016; Carniani et al. 2018a; Smit et al. 2018; Hashimoto et al. 2019; Matthee et al. 2019; Bakx et al. 2020; Harikane et al. 2020; Le Fèvre et al. 2020; Bouwens et al. 2021; Fudamoto et al. 2021). The widespread interest in detecting the [CII] emission from local and distant galaxies is highly justified. This is the brightest line arising from the rest-frame far-infrared (FIR) spectra of star-forming galaxies (SFGs), representing one of the main coolants of their interstellar medium (ISM; e.g., Stacey et al. 1991; Carilli & Walter 2013). The bulk of its emission originates from photo-dissociation regions (PDRs; Hollenbach & Tielens 1999), possibly tracing the formation of new stars from giant molecular clouds. However, given its low ionization potential (11.3 eV, compared to the 13.6 eV of neutral hydrogen), this line deserves a thoughtful physical interpretation as it can also trace the diffuse neutral medium (e.g., Wolfire et al. 2003; Vallini et al. 2015), the molecular (e.g., Zanella et al. 2018; Dessauges-Zavadsky et al. 2020), and ionized (e.g., Cormier et al. 2012) gas. Furthermore, there is evidence that [CII] can reasonably trace the total HI content of galaxies (Heintz et al. 2021). The continuum surrounding this line lies close to the peak of the FIR dust emission,

making detections easier and helping to constrain the total FIR luminosity and obscured star formation (e.g., Gruppioni et al. 2020; Khusanova et al. 2021; Pozzi et al. 2021). Moreover, the [CII] emission can provide important information on a variety of ISM properties, such as the star-formation rate (SFR; e.g., De Looze et al. 2014; Olsen et al. 2017), the presence of outflows (e.g., Gallerani et al. 2018; Ginolfi et al. 2020), and the kinematics of the ISM (e.g., Jones et al. 2021; Romano et al. 2021). Therefore, the comparison of [CII] observations with simulations is mandatory to disentangle the diverse processes that take place in galaxies in order to understand how they shape the observed morphology and kinematics of the line (e.g., Vallini et al. 2017; Ferrara et al. 2019; Kohandel et al. 2019).

In this context, the ALMA Large Program to INvestigate [CII] at Early times (ALPINE) survey (Béthermin et al. 2020; Faisst et al. 2020; Le Fèvre et al. 2020) has recently provided the first statistically significant sample of high-redshift normal¹ galaxies detected in [CII] at the end of the reionization epoch ($4.4 < z < 5.9$). ALPINE observed a sample of 118 SFGs selected in UV and with redshifts spectroscopically confirmed by previous campaigns (Le Fèvre et al. 2015; Tasca et al. 2017; Hasinger et al. 2018) in order to ensure precise detections of the [CII] line. In particular, considering those galaxies with a [CII] emission $\geq 3.5\sigma$ as detections (corresponding to a 95% sample

¹ These galaxies lie along a well-defined “star-forming main-sequence”, with a relatively tight dispersion (< 0.3 dex) in the SFR versus stellar mass plane (e.g., Noeske et al. 2007; Rodighiero et al. 2011; Speagle et al. 2014).

[†] Deceased.

purity), ALPINE reached a successful rate of 64%, resulting in 75 detections and 43 nondetections (B  thermin et al. 2020; Le F  vre et al. 2020).

B  thermin et al. (2020) first investigated the $L_{\text{[CII]}}$ -SFR relation by taking advantage of the ALPINE continuum-detected galaxies. They computed the average SFRs in different [CII] luminosity bins as the sum of the UV rest-frame data (Faisst et al. 2020) and of the mean obscured SFRs derived through the stacking of the continuum data (i.e., $\text{SFR}_{\text{total}} = \text{SFR}_{\text{UV}} + \text{SFR}_{\text{IR}}$). Their results are in good agreement with the local and predicted relations. Then, Schaerer et al. (2020) took advantage of the full ALPINE sample, including both [CII]-detected galaxies and upper limits on nondetections (see Sect. 4), to study the evolution of the $L_{\text{[CII]}}$ -SFR relation over cosmic time and to understand if the [CII] line is a good tracer of the SFR at high redshift as it is in the local Universe (e.g., De Looze et al. 2014; Pineda et al. 2014). They found that the [CII] luminosity of the ALPINE galaxies scales linearly with their total SFRs (as traced by the sum of UV and IR contributions; see Schaerer et al. 2020), with a slight steepening of the slope depending on the [CII] nondetections upper limits used (B  thermin et al. 2020). However, to fully establish the connection between $L_{\text{[CII]}}$ and SFR in distant galaxies, a more in depth investigation of the ALPINE nondetections is needed.

In this work, we derive the average properties of the population of [CII] undetected galaxies in ALPINE through line stacking and use them to investigate the [CII] as a tracer of SFR at high redshift, and to put additional constraints on the already thoroughly studied $L_{\text{[CII]}}$ -SFR relation (Schaerer et al. 2020).

The structure of the paper is the following: in Sect. 2 we introduce the available data and observations used to compute the [CII] line profile resulting from the average population of nondetections. The procedure adopted to obtain the stacked line is described in Sect. 3. The results are reported in Sect. 4 and discussed in Sect. 5, respectively. Summary and conclusions are provided in Sect. 6.

Throughout this work, we adopt a Λ -CDM cosmology with $H_0 = 70 \text{ km s}^{-1} \text{ Mpc}^{-1}$, $\Omega_m = 0.3$ and $\Omega_\Lambda = 0.7$. Furthermore, we use a Chabrier (2003) initial mass function (IMF).

2. Data and observations

2.1. Multiwavelength and ALMA data

The ALPINE survey was designed to observe the [CII] line at $158 \mu\text{m}$ rest-frame and the surrounding FIR continuum emission from a sample of 118 SFGs at $4.4 < z < 5.9$, avoiding the redshift range $4.6 < z < 5.1$ due to a low-transmission atmospheric window. The campaign spent ~ 70 h of observation in ALMA Band 7 (275–373 GHz) during cycles 5 and 6. The targets are drawn from the well-studied Cosmic Evolution Survey (COSMOS; Scoville et al. 2007a,b) and Extended Chandra Deep Field South (E-CDFS; Giavalisco et al. 2004; Cardamone et al. 2010) fields and have been observed in large optical/near-infrared (NIR) spectroscopic campaigns such as VIMOS Ultra-Deep Survey (VUDS; Le F  vre et al. 2015; Tasca et al. 2017) and DEIMOS 10K Spectroscopic Survey (Hasinger et al. 2018). They are selected in the rest-frame UV ($L_{\text{UV}} > 0.6 L^*$) and lie on the main-sequence, thus being representative of the average population of SFGs at $z \sim 5$ (e.g., Speagle et al. 2014). A wealth of multiwavelength data is available for these sources, from the UV to the NIR (e.g., Koekemoer et al. 2007; Sanders et al. 2007; McCracken et al. 2012; Guo et al. 2013; Nayyeri et al. 2017), allowing us to recover physical quantities such as

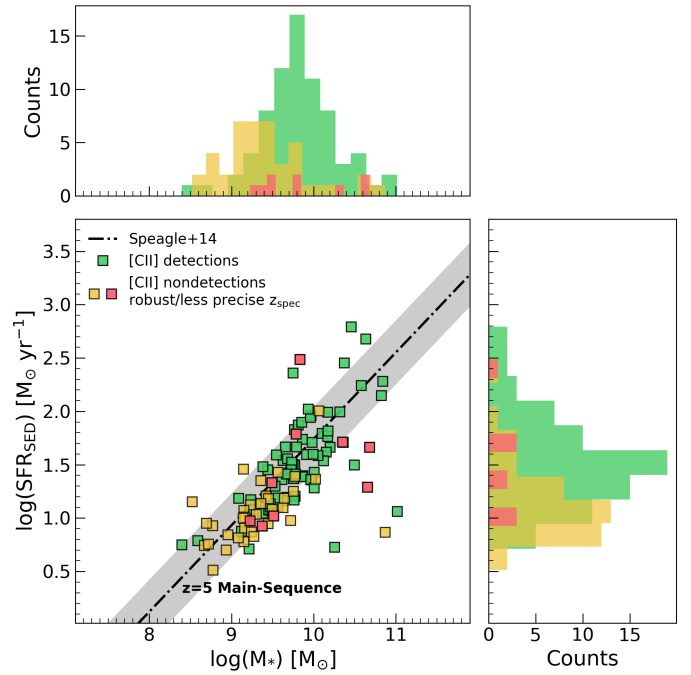


Fig. 1. SFRs vs stellar masses of the ALPINE [CII]-detected (green squares) and undetected (yellow squares) galaxies. Red symbols represent [CII] nondetections with less precise spectroscopic redshift (see Sect. 2.2). The main-sequence of star-forming galaxies by Speagle et al. (2014) is shown as the black dot-dashed line, with its ± 0.3 dex width represented by the gray shaded region. Top and right panels report the distributions in stellar mass and SFR, respectively, for both the detections and nondetections.

stellar masses ($9 \lesssim \log(M_*/M_\odot) \lesssim 11$) and star-formation rates ($1 \lesssim \log(\text{SFR}/M_\odot \text{yr}^{-1}) \lesssim 3$) through spectral energy distribution (SED)-fitting (Faisst et al. 2020). Data are also available in the X-ray and radio bands (e.g., Hasinger et al. 2007; Smol  i   et al. 2017).

The ALMA data cubes were reduced and calibrated using the standard Common Astronomy Software Applications (CASA; McMullin et al. 2007) pipeline. Each cube was continuum-subtracted in the uv -plane in order to obtain line-only cubes with channel width of $\sim 25 \text{ km s}^{-1}$ and beam size of $\sim 1''$ (with a pixel scale of $\sim 0.15''$; B  thermin et al. 2020). A line search algorithm was then applied to each continuum-subtracted cube resulting in 75 [CII] detections (signal-to-noise ratio; $S/N > 3.5$) and 43 nondetections. In Fig. 1 we show the distributions of [CII]-detected and undetected galaxies along the $z \sim 5$ main-sequence of SFGs. The stellar masses and SFRs are those from the SED-fitting (Faisst et al. 2020). As evident, the ALPINE nondetections lie on the bottom-left side of the main-sequence, at lower stellar masses and SFRs with respect to those detected in [CII] (except for a few massive sources below the sequence).

For a more in-depth description of the overall ALPINE survey, the observations, data processing, and multiwavelength analysis see Le F  vre et al. (2020), B  thermin et al. (2020), and Faisst et al. (2020), respectively.

2.2. Rest-frame UV spectroscopic data

The 118 ALPINE galaxies have confirmed rest-frame UV spectroscopic redshifts from the VUDS (Le F  vre et al. 2015; Tasca et al. 2015) and DEIMOS 10K (Hasinger et al. 2018) surveys. These are obtained both from the $\text{Ly}\alpha$ line and from UV

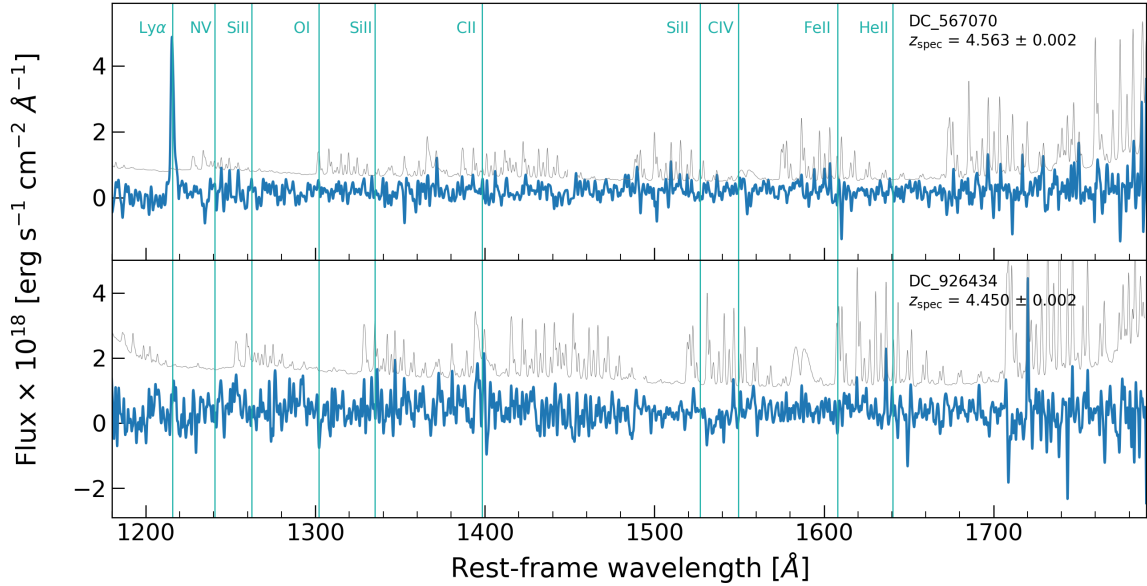


Fig. 2. Examples of optical spectra of two [CII] nondetections with robust (*top*) and less precise (*bottom*) rest-frame UV spectroscopic redshift. The typical redshift uncertainty due to the spectral resolution (i.e., $R \sim 2700$ from [Hasinger et al. 2018](#)) of the observations is also shown. Both panels report UV emission and absorption features, such as the $\text{Ly}\alpha$ line or the ISM Si II, C IV and He II absorption lines. The spectra (in blue) and the noise (in gray) are smoothed with a Gaussian filter with size of 2 \AA for a better visualization of the emission and absorption features.

rest-frame ISM absorption lines. However, these features are not always the best tracers of the systemic redshift of a source. The $\text{Ly}\alpha$ emission line is typically redshifted (with respect to the systemic velocity) because of the resonant scattering of the $\text{Ly}\alpha$ photons (e.g., [Dijkstra 2014](#); [Verhamme et al. 2015](#)). On the opposite, ISM lines are usually blueshifted, suggesting the presence of outflowing gas (e.g., [Steidel et al. 2010, 2018](#)). The [CII] line is not affected by this kind of issues and, in principle, it can be used to stack together the ALMA spectra of the ALPINE nondetections to search for a significant signal. Moreover, it is not absorbed by dust and can be observed across the entire galaxy, resulting in a better tracer of the systemic redshift than optical nebular lines (e.g., [Cassata et al. 2020](#); [Faisst et al. 2020](#)).

We do not have the systemic redshift information for the 43 ALPINE nondetections, therefore we can just rely on their UV redshifts. In particular, we need to know the UV spectroscopic redshifts of our sources with good accuracy in order to exclude objects with less precise redshift estimates for which the [CII] line could lie outside of the ALMA observational window or that could alter the $\Delta v_{\text{Ly}\alpha}$ statistics in our stacking analysis (see Sect. 3). For this reason, we visually inspected the optical spectra of the nondetections. We found that 34 out of 43 sources present multiple high S/N spectral features, all of them showing a prominent $\text{Ly}\alpha$ line in emission, allowing for a precise and accurate estimate of their spectroscopic redshifts. The remaining nine galaxies have very weak or no $\text{Ly}\alpha$ in emission² and less prominent and sharp UV absorption lines. Although it is likely that the redshift is generally accurate for these sources as well, we decided to exclude them from our stacking analysis, in order not to include additional uncertainties due to possible strong [CII] offsets with respect to the expected position of the line. Figure 2 reports an example of UV/optical spectra of two [CII] nondetections with a robust and less precise spectroscopic

redshift, respectively. In the first case, the galaxy shows a clear $\text{Ly}\alpha$ line in emission and some other possible absorption features at longer wavelengths that provide a precise estimate of the spectroscopic redshift. On the other hand, the spectrum of the second source is quite noisy, with fewer recognizable spectral features. We thus obtain a final sample of 34 [CII] nondetections. The rest-frame UV and ALMA emissions of these galaxies are shown in Fig. 3, where it is evident that no significant [CII] signal is present in these sources³. The nine galaxies with less precise z_{spec} are also reported for completeness in Fig. 1 as red squares.

For these reasons, in the following analysis, we make use of the redshift obtained from the peak of the $\text{Ly}\alpha$ line, and then correct it for the observed velocity offsets between $\text{Ly}\alpha$ and the systemic velocity traced by [CII] ($0 < \Delta v_{\text{Ly}\alpha} < 400 \text{ km s}^{-1}$) for the ALPINE detections ([Cassata et al. 2020](#)).

3. Stacking of nondetections

We proceeded with a mean stacking of the ALMA spectra of the 34 ALPINE [CII] nondetections to search for a signal emerging from the noise of individual galaxies. In principle, the stacking analysis can be done both in the image and uv planes. In the first case, it is possible to perform both 1D and 3D stacking through the extraction of individual spectra and by exploring the full data cubes, respectively (e.g., [Bischetti et al. 2019](#); [Stanley et al. 2019](#)). 2D stacking can be performed as well, by aligning and summing intensity maps of different sources (e.g., [Méndez-Hernández et al. 2020](#)). The stacking in the uv plane is instead based on the analysis of the visibility data associated with the emission line in the Fourier space, before the imaging process (e.g., [Fujimoto et al. 2019](#); [Carvajal et al. 2020](#)). [Lindroos et al. \(2015\)](#) made use of several simulated uv

² We note that there are many factors that could absorb and/or decrease the $\text{Ly}\alpha$ emission, such as the presence of dust and its geometrical distribution, or the clumpiness of the ISM (e.g., [Dijkstra 2014](#); [Messa et al. 2019](#); [Cassata et al. 2020](#)).

³ A few maps show a 3σ [CII] emission in spatial coincidence with the rest-frame UV emission. Although these sources present signs of significant [CII] content, they were classified as nondetections given their S/N smaller than 3.5σ (see Sect. 2.1).

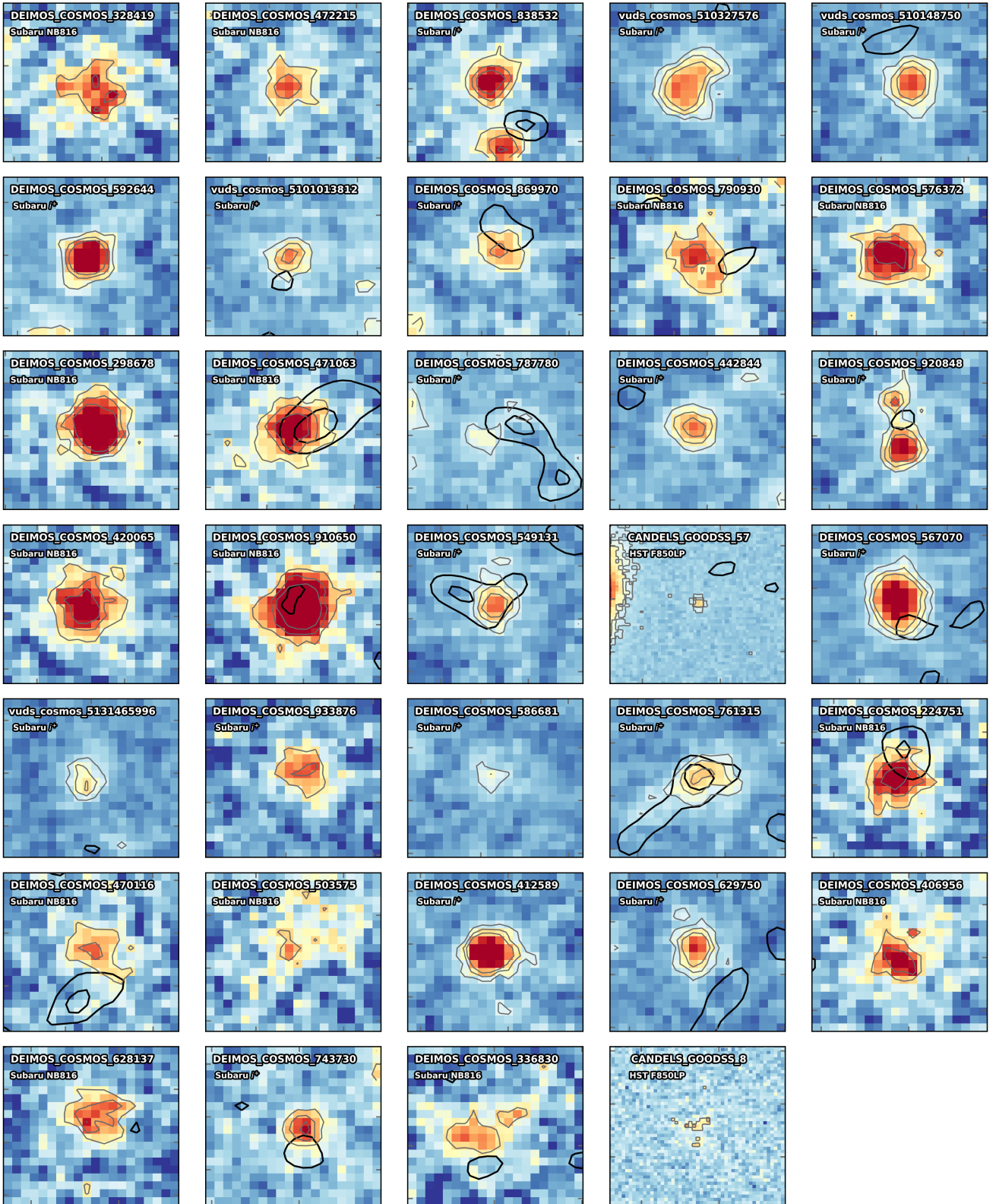


Fig. 3. Cutouts of the 34 [CII] nondetections centered on their optical positions. Depending on the method used to preselect each galaxy before the spectroscopic observation, that is Lyman-break, $\text{Ly}\alpha$, or i -band dropout selection, we show the emission from the Subaru broad-band i^+ and narrow-band NB816 filters (Taniguchi et al. 2007, 2015; Laigle et al. 2016), or from the HST/ACS F850LP (Giavalisco et al. 2004), respectively (see Faisst et al. 2020). Each image is $3'' \times 3''$ wide. Gray contours show 3, 5, and 7σ optical emission. Black contours (if present) represent 2 and 3σ ALMA [CII] emission. The name of each nondetection, as well as the filter used, are reported in the upper-left corner of the corresponding cutout.

continuum data sets to compare the performances of image and uv stacking. They found that the two procedures yield similar results within the uncertainties, although in some cases stacking in the uv plane could lead to higher S/N, also avoiding possible issues during the deconvolution process from the Fourier to the image domain. Méndez-Hernández et al. (2020) also made a comparison between the image and uv stacking of CO emission lines in a sample of 27 low- z SFGs drawn from the Valparaíso ALMA/APEX Line Emission Survey (VALES; Villanueva et al. 2017; Cheng et al. 2018). They retrieved similar flux densities with both methods, with the uv stacking producing similar or slightly higher S/N as compared to the image one, depending on the brightness of the line. Regardless of the adopted method, all the above techniques need a good knowledge of the systemic redshift of the source. Furthermore, to select the spectral channels including the emission line in the case of uv stacking or for the production of the intensity maps, an estimate of the full width at half maximum (FWHM) of each source is also required. In the analysis of the ALPINE [CII] undetected galaxies, we do not know at which frequency the expected line is (because of the observed velocity offset between Ly α and [CII]), and we do not have any information on the FWHM of each source. For these reasons, and considering that both image and uv planes provide similar results, we decided to proceed with a 1D spectral stacking of the [CII] nondetections starting from the image plane.

In particular, we extracted each spectrum from the original data cubes of the ALPINE data release 1 (DR1; Béthermin et al. 2020)⁴, within a fixed aperture of 1'' of radius (defining the central regions of the ALPINE targets; see Béthermin et al. 2020) centered at the optical position of the source⁵, and covering a spectral range of ~ 3 GHz around the expected peak frequency of the emission line (as traced by the Ly α emission). At first, we used the Ly α -based spectroscopic redshifts of the nondetections to align them to the same reference frame, and then we stacked them together. Because the Ly α line is typically shifted to the red relative to the systemic redshift as defined by the [CII] line (Cassata et al. 2020), it was likely that our stacked emission was offset from the systemic by some amount. Further, the velocity offset between Ly α and systemic is not constant, but is rather a complicated function of various physical conditions within a given galaxy (e.g., Erb et al. 2004; Pentericci et al. 2016; Marchi et al. 2019), meaning that the signal recovered in a stack where these offsets were not accounted for would be broadened and dampened. For these reasons, we applied to each source a spectral offset randomly extracted from the $\Delta v_{\text{Ly}\alpha}$ distribution obtained by Cassata et al. (2020) from a subsample of the ALPINE detections, and then we computed the mean stack on the shifted spectra. Certainly, by drawing random values out of the $\Delta v_{\text{Ly}\alpha}$ distribution we expected to introduce an artificial broadening of the stacked line, as well. In particular, the further (nearer) the rest-frame UV spectroscopic redshift (as traced by the Ly α line) from the systemic one (as traced by the [CII] line), the wider (narrower) the stacked line. To avoid this issue, we computed each time a Gaussian fit on the stacked line, estimating its full width at half maximum as $FWHM = 2.355\sigma$, where σ is the standard deviation of the Gaussian. For each stacked spectrum, we then required that $FWHM \leq 400 \text{ km s}^{-1}$,

⁴ DR1 data are available at https://cesam.lam.fr/a2c2s/data_release.php.

⁵ The coordinates of each galaxy are taken either from the COSMOS2015 (Laigle et al. 2016) or 3D-HST (Brammer et al. 2012; Skelton et al. 2014) catalogs, depending on which field (COSMOS or E-CDFS) the source is located (see Faisst et al. 2020 for more information).

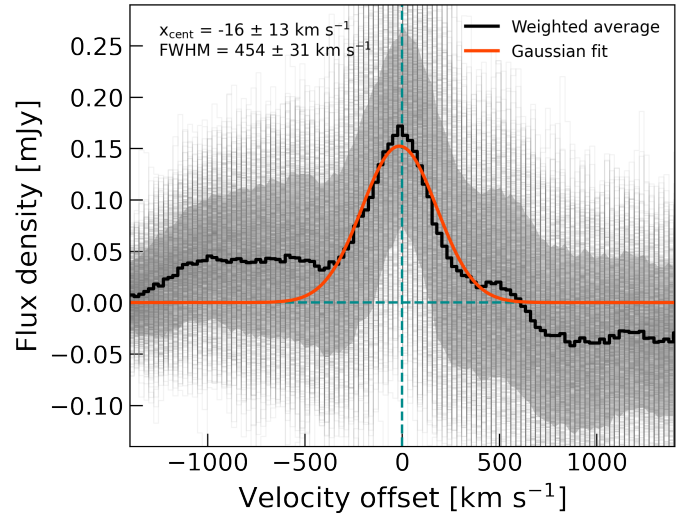


Fig. 4. Average spectrum of the ALPINE [CII] nondetections weighted for the S/N of the individual stacked spectra with $FWHM \leq 400 \text{ km s}^{-1}$ (solid black line). The thin lines represent the individual realizations after taking into account the observed shift between the [CII] and Ly α lines (Cassata et al. 2020). The solid red line represents the Gaussian fit on the average line profile. The shaded area shows the uncertainty associated with the average line profile as taken from the 16th and 84th percentiles of the 1000 spectra distribution. The dashed dark cyan lines mark the zero flux and velocity offset levels. The centroid and FWHM computed from the Gaussian fit on the average line profile are shown on the top left corner.

which defines the 84th percentile of the observed FWHM distribution of the ALPINE [CII] detections (see Béthermin et al. 2020), until reaching 1000 realizations.

We show the result of this procedure in Fig. 4, where the gray histograms represent the spectra that satisfy the above requirements on the FWHM. To produce the averaged line profile, we weighted each realization of the stacked spectra in different ways. We assumed $w = 1$ in case of no weighting, $w = 1/\sigma_{\text{rms}}^2$ for an inverse-variance weighting (where σ_{rms} is the standard deviation of each stacked spectrum)⁶, and $w = S/N$ to weight each stacked spectrum by its S/N. In the latter case, we estimated the S/N as the ratio between the peak flux of the stacked line and the standard deviation of the spectral channels at velocities greater and smaller than $\pm 600 \text{ km s}^{-1}$ from the peak, in order to avoid contamination from the stacked emission line. The line profiles obtained by applying these different weightings are similar to each other, although resulting in a slightly higher S/N for the case with $w = S/N$. For this reason, we decide to show in Fig. 4 only the average stacked spectrum obtained by weighting each realization by its S/N.

We then checked the effect of the random extraction on the final average stacked profile by making the following test. We selected a subsample of [CII] detections having, in addition to the [CII]-traced systemic redshift, also the redshift

⁶ We checked that the integrated flux and S/N of the final average stacked line do not change significantly if we weight the individual spectra by their observed rms in each realization. In the latter case, we obtained indeed a slightly lower flux (resulting in a ~ 0.1 dex lower [CII] luminosity) and similar S/N if compared to those computed with our method, that is by directly weighting the stacked spectra of each realization for their rms. The two methods provide comparable results likely because of the distributions of the individual rms of our 34 spectra, that are quite constant in both of the two ALPINE redshift bins of our sample, providing similar weights to each source in the stack.

measurements from Ly α . We first stacked together the ALMA spectra basing on their systemic redshifts (i.e., without applying any spectral offset) to obtain the real FWHM and flux of the line. Then, we repeated the stacking by using our method, that is by extracting random shifts from the $\Delta v_{\text{Ly}\alpha}$ distribution, and we compared the two results. We found that the random extraction method produces a ~ 2 times broader FWHM than the true value computed by stacking the spectra at their correct wavelengths. At the same time, there is no significant difference in the retrieved S/N and integrated fluxes. As an additional check, we repeated the entire stacking procedure by considering, for each source, the mean value of the Ly α -[CII] offset distribution found by Cassata et al. (2020) (i.e., ~ 183 km s $^{-1}$), obtaining a FWHM ~ 150 km s $^{-1}$ narrower than what previously found. On the other hand, the integrated flux and S/N of the resulting line are slightly lower, but still comparable, than those computed by assuming the random $\Delta v_{\text{Ly}\alpha}$ offsets. This further suggests that the random extraction has only a significant effect on the FWHM of the stacked line. Therefore, we are confident that the stacking method used in this work does not under/overestimate the true value of the [CII] luminosity of the population of nondetections under study.

By fitting the stacked line profile with a Gaussian function, we found the signal peaking at $x_{\text{cent}} = -16 \pm 13$ km s $^{-1}$, consistent with the systemic velocity traced by the [CII] line, and having $\text{FWHM} = 454 \pm 31$ km s $^{-1}$. The computed S/N is ~ 5.1 , revealing the presence of an underlying population of [CII] emitters likely suffering from low S/N (in terms of [CII] emission) possibly caused by the low SFRs and stellar masses which characterize them (see Fig. 1). Following Solomon et al. (1992), we also computed $L_{[\text{CII}]}$ as

$$L_{[\text{CII}]} = 1.04 \times 10^{-3} S_{[\text{CII}]} \Delta v D_L^2 \nu_{\text{obs}} [L_{\odot}], \quad (1)$$

where $S_{[\text{CII}]} \Delta v$ is the velocity-integrated line flux in units of Jy km s $^{-1}$, D_L is the luminosity distance in Mpc at the median redshift of the sample (i.e., $z_{\text{med}} = 5.52$), and ν_{obs} is the observed peak frequency in Gigahertz.

To attribute an uncertainty on the velocity-integrated flux (and hence on the [CII] luminosity) we performed a deleted jackknife resampling (Shao & Wu 1989). We produced 500 jackknife realizations following the same method described above, but randomly removing each time 20%⁷ of the 34 spectra in the parent sample and computing again the integrated flux of the stacked spectra. The error on $S_{[\text{CII}]} \Delta v$ was then computed from the 16th and 84th percentiles of the fluxes distribution of the 500 jackknife realizations. As a result, we obtained $S_{[\text{CII}]} \Delta v = (73 \pm 11) \times 10^{-3}$ Jy km s $^{-1}$.

We thus found $\log(L_{[\text{CII}]} / L_{\odot}) = 7.8 \pm 0.3$, where the error was computed by propagating the uncertainty on the [CII] flux and the redshift on Eq. (1). We tested that this result is not significantly different from the one obtained by removing the constraint on the FWHM of the stacked spectra, which thus affects only the width of the line.

Furthermore, given the wide range spanned by the [CII] nondetections both in stellar mass (i.e., $9 \lesssim \log(M_*/M_{\odot}) \lesssim 11$) and star-formation rates (i.e., $0.5 \lesssim \log(\text{SFR}/M_{\odot}\text{yr}^{-1}) \lesssim 2.0$; see Fig. 1), we decided to split our sample in two bins of SFR to check if the above result from stacking was dominated by the most massive and star-forming sources. We used the median SFR of the sample ($\log(\text{SFR}_{\text{TOT,med}}/M_{\odot}\text{yr}^{-1}) = 1.16$; as defined in

⁷ This percentage represents a good compromise in using the jackknife method to estimate the error on our measurements while still having a reasonable number of sources to stack at each time (Efron 1982).

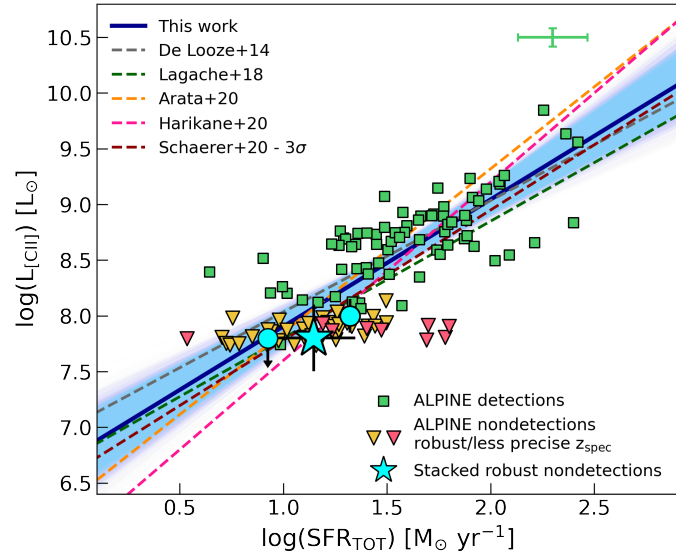


Fig. 5. [CII] luminosity as a function of total SFR (UV+FIR; see text) for the ALPINE detections (green squares) and nondetections (as 3σ upper limits; yellow triangles). The red markers represent the [CII]-undetected galaxies with less precise z_{spec} (see Sect. 2). The green errors in the upper right corner show the average uncertainties of [CII] detections on both $L_{[\text{CII}]}$ and SFR. The cyan big star shows the result of this work for the stacked nondetections, with the error on $L_{[\text{CII}]}$ computed as described in Sect. 3. The cyan circles are the [CII] upper limit and detection found in the low- and high-SFR bins introduced in the text, respectively. We also report different $L_{[\text{CII}]}$ -SFR relations from the literature: the local relation by De Looze et al. (2014) (dashed gray line), the predicted relation by the models of Lagache et al. (2018) at $z \sim 5$ (dashed green line), the predicted relation by Arata et al. (2020) for galaxies at $z > 6$ (dashed yellow line), the fitted relation by Harikane et al. (2020) on $z > 6$ galaxies (dashed pink line), the latest results obtained by Schaefer et al. (2020) at $z \sim 5$ with ALPINE considering nondetections as 3σ upper limits (dashed red line). Finally, the solid blue line and shaded area report our best-fit and uncertainties to the [CII] detections + stacked robust nondetections.

Sect. 4) to make two bins composed of 17 objects each, repeating for both of them the previously described stacking procedure. We did not find any significant emission in the low-SFR bin. On the contrary, a S/N ~ 6.8 emission was produced in the high-SFR bin, suggesting that most of the signal in Fig. 4 is due to the most massive SFGs. By adopting the above-described stacking procedure on the whole sample, we found $\log(L_{[\text{CII}]} / L_{\odot}) = 8.0 \pm 0.2$ in the high-SFR bin. In the lower bin with no detection, we considered instead the average of the [CII] nondetections with robust spectroscopic redshift, computed as the addition in quadrature of the corresponding [CII] upper limits divided by the square root of the number of sources in the bin (e.g., Cohen 1988), finding $\log(L_{[\text{CII}]} / L_{\odot}) \lesssim 7.8$. We show these results in Fig. 5, along with the previous result from the stacking of all the [CII] nondetections.

Finally, Fig. 4 shows that the average [CII] profile presents a negative (positive) continuum at the right (left) of the line. By analyzing each spectrum individually, we attributed this behavior to different sources that present a negative (positive) continuum at positive (negative) velocity offset with respect to the expected line. However, we believe that this issue is only due to statistical fluctuations originated from the small size of the sample, rather than to calibration problems in the ALMA data reductions or physical processes in these sources. This is also confirmed by the dispersion of the 1000 realizations of the

Table 1. Summary of $L_{\text{[CII]}}$ -SFR relations from the literature and from this work, as parameterized in Eq. (2).

Literature (1)	Sample (2)	Redshift (3)	a (4)	b (5)
De Looze et al. (2014)	HII/starburst	<0.5	7.06 ± 0.33	1.00 ± 0.04
Lagache et al. (2018)	G.A.S. + CLOUDY	4 – 6	6.75 ± 0.07	1.05 ± 0.07
Arata et al. (2020)	GADGET-3 + ART ²	>6	6.38	1.47
Harikane et al. (2020)	LBGs/SMGs	6 – 9	6.00	1.60
Schaerer et al. (2020)	ALPINE (3σ limits)	4 – 6	6.61 ± 0.20	1.17 ± 0.12
This work	ALPINE det + stacked non-det	4 – 6	6.76 ± 0.17	1.14 ± 0.11

stacked line in the figure, which shows that the above-mentioned continuum levels are not significant and consistent with zero.

4. Results

By taking advantage of the [CII] luminosity computed from the stack of the ALPINE nondetections, we explored the relation between $L_{\text{[CII]}}$ and SFR in these galaxies in order to compare them to the results obtained for the combined [CII] detections and nondetections upper limits (Schaerer et al. 2020).

Following Schaerer et al. (2020), we report in Fig. 5 the [CII] luminosities and SFRs of the ALPINE detections and nondetections (as 3σ upper limits; see also Fig. 4 by Schaerer et al. 2020). Contrarily to Fig. 1 in which we show the SFRs obtained through SED-fitting (for consistency with the stellar mass values obtained with the same procedure; Faisst et al. 2020), we use in this case the total SFRs obtained as $\text{SFR}_{\text{TOT}} = \text{SFR}(\text{UV}) + \text{SFR}(\text{IR})$, where $\text{SFR}(\text{UV})$ comes from the observed UV absolute magnitude at 1500 Å, and $\text{SFR}(\text{IR})$ is obtained both through the ALMA continuum measurements and, for galaxies undetected in continuum, through predictions of the IRX- β relation by Fudamoto et al. (2020)⁸, obtained from a stacking analysis of all ALMA continuum images, including both individual detections and nondetections. In this way, we are able to compare our results with those previously found in ALPINE by Schaerer et al. (2020) and with other $L_{\text{[CII]}}$ -SFR relations already present in the literature. Among these, we show: (i) the local $L_{\text{[CII]}}$ -SFR relation found by De Looze et al. (2014) for a sample of low- z HII/starburst galaxies⁹; (ii) the predicted relation found by Lagache et al. (2018) at $z = 5$; (iii) the predictions from simulations for $z > 6$ galaxies by Arata et al. (2020); (iv) the relation found by Harikane et al. (2020) for galaxies observed in [CII] at $6 < z < 9$; (v) the relation fitted to the ALPINE data only (including 3σ upper limits on nondetections) by Schaerer et al. (2020). Furthermore, we show our results from the stacking of ALPINE [CII] nondetections (i.e., $\log(L_{\text{[CII]}}/L_{\odot}) = 7.8 \pm 0.3$), adopting their mean SFR_{TOT} (i.e., $\log(\text{SFR}_{\text{TOT,mean}}/M_{\odot} \text{ yr}^{-1}) = 1.14 \pm 0.20$ ¹⁰, that is also in good agreement with the upper limit found by Béthermin et al. (2020) by stacking the ALMA continuum of the [CII] nondetections. For further information, see their Section 7.5). For comparison, we also report the [CII]

⁸ It is worth to specify that none of our 34 [CII] nondetections is detected in continuum. Therefore, the $\text{SFR}(\text{IR})$ for all of these galaxies comes from the IRX- β relation by Fudamoto et al. (2020).

⁹ As this relation is based on a Kroupa & Weidner (2003) IMF, we scaled it to a Chabrier (2003) IMF by dividing the SFR by a factor 1.06 (e.g., Madau & Dickinson 2014), for consistency with other measurements from the literature.

¹⁰ The error on $\text{SFR}_{\text{TOT,mean}}$ is computed from the 16th and 84th percentiles of the SFR_{TOT} distribution of the [CII] nondetections.

upper-limit and detection found in the low- and high-SFR bin respectively, as described in Sect. 3.

Our $L_{\text{[CII]}}$ value is consistent with the 3σ upper limits found by Béthermin et al. (2020) and used by Schaerer et al. (2020) in their analysis. This result suggests that the [CII] nondetections are not drawn from a different population of galaxies with respect to the ALPINE detections. Rather, these are galaxies lying on the bottom-left region of the $z \sim 5$ main-sequence with lower SFRs and stellar masses, and possibly with fainter [CII] emission (see also Sect. 5 for possible caveats causing low [CII] content in high- z galaxies).

We fitted the combined [CII] luminosity and SFR from the stacking of nondetections with the ALPINE [CII]-detected galaxies with a linear relation of the form

$$\log(L_{\text{[CII]}}/L_{\odot}) = a + b \times \log(\text{SFR}/M_{\odot} \text{ yr}^{-1}), \quad (2)$$

where a and b are the intercept and slope of the relation, respectively. For consistency with Schaerer et al. (2020), we used the `linmix` package¹¹ by Kelly (2007) which makes use of a Bayesian approach to account for measurement errors in both variables in linear regressions. The errors on the [CII] luminosities are taken from Béthermin et al. (2020) for the ALPINE detections, and from the stacking for the nondetected sources. Regarding the individual uncertainties on the SFRs, we propagated the errors of $\text{SFR}(\text{UV})$ and $\text{SFR}(\text{IR})$ on the total SFR (obtaining on average ~ 0.2 dex for both detections and nondetections).

With our stacked nondetections, we obtain a best-fit relation with $a = 6.76 \pm 0.17$ and $b = 1.14 \pm 0.11$. This is consistent with the slope obtained from local galaxies ($b = 1.00 \pm 0.04$; De Looze et al. 2014), and in agreement with that previously found by Schaerer et al. (2020) considering detections and 3σ upper limits on nondetections (i.e., $b = 1.17 \pm 0.12$). Table 1 summarizes the parameters describing the $L_{\text{[CII]}}$ -SFR relations found in the literature and in this work.

5. Discussion

A large scatter in the $L_{\text{[CII]}}$ -SFR relation is in place for sources at $z > 4$ (i.e., $\gtrsim 0.4$ dex, that is ~ 2 times larger than the intrinsic dispersion of local galaxies; Carniani et al. 2018b; Schaerer et al. 2020). Such a scatter is produced by the multitude of [CII] detections and nondetections now available in the high- z Universe, and could be due both to different physical conditions in the ISM of distant galaxies, or to systematic in the [CII] and SFR derivation.

Jolly et al. (2021) analyzed a sample of 52 gravitationally lensed galaxies at $z \gtrsim 6$ as part of the ALMA Lensing

¹¹ <https://github.com/jmeyers314/linmix>.

Cluster Survey (ALCS) searching for [CII] emission through spectral stacking. They found no [CII] detection in their sample, providing 3σ upper limits on the [CII] luminosity of $\log(L_{[\text{CII}]} / L_{\odot}) < 7-8$, depending on the considered subsample (e.g., sources with high SFR, or with secure spectroscopic redshift) and stacking method (i.e., weighted mean and median stacking)¹². Their findings are comparable¹³ with (or lower than) our average [CII] luminosity from the ALPINE nondetections (i.e., $\log(L_{[\text{CII}]} / L_{\odot}) = 7.8 \pm 0.3$). However, these authors claim that the [CII] upper limits they found could be underestimated because some potential biases in the analyzed galaxy sample. First, they do not account for the spectroscopic offset between $\text{Ly}\alpha$ and [CII] that, as mentioned in Sect. 3, could alter the stacked line profile and lower the average amount of [CII] luminosity arising from nondetections. Astrometric offsets between ALMA and ancillary data could affect the [CII] luminosity estimate, as well. This issue was well-studied by many authors in the literature (e.g., Dunlop et al. 2017; Franco et al. 2018), and in ALPINE by Faisst et al. (2020) and Fujimoto et al. (2020), who found a typical shift between [CII] and UV rest-frame emission of $0.15''$ (corresponding to ~ 1 kpc at $z = 5$). We overcome this problem by considering a fixed aperture of $1''$ of radius to extract the ALMA spectra of the [CII] nondetections (which is also ~ 3 times larger than the typical [CII] size of individual detections in ALPINE, i.e., 2.1 kpc). The surface brightness distribution of the [CII] emission and its FWHM could also reduce the [CII] luminosity and cause nondetections. For instance, Fujimoto et al. (2020) found that [CII] emission is typically 2–3 times more extended than rest-frame UV emission, which could result in a large underestimation of the total [CII] flux, depending on the resolution of the observations (e.g., Carniani et al. 2020). Kohandel et al. (2019) studied instead the effect of FWHM and inclination of the galaxy on the [CII] detectability, finding that an edge-on galaxy with a large line width (i.e., $\text{FWHM} > 400 \text{ km s}^{-1}$) could result in a nondetection, biasing the [CII] luminosity estimates in high- z sources. Finally, Jolly et al. (2021) noticed that their results may be lowered by the presence of a large number of $\text{Ly}\alpha$ emitters in their sample, that could in principle have small content of dust, resulting in low [CII] and FIR emission. This issue has been minimized in the ALPINE sample by a heterogeneous preselection of the spectroscopically observed galaxies done with a variety of diverse selection methods (Faisst et al. 2020). In addition, Cassata et al. (2020) found that 44% of the ALPINE sources are $\text{Ly}\alpha$ emitters¹⁴, with the probability of detecting [CII] not strongly dependent on the presence of bright $\text{Ly}\alpha$ emission.

Apart from the above caveats, the little [CII] content found by Jolly et al. (2021) in their galaxies could also be due to low metallicity levels. Indeed, many simulations show that low metallicity in high- z galaxies could result in a lower Carbon abundance, and stronger radiation field that could decrease the [CII] content (e.g., Vallini et al. 2015, 2020; Ferrara et al. 2019).

¹² It is worth saying that Jolly et al. (2021) did not find a significant difference between their mean and median stacked cubes. Rather, most of the discrepancy in their two methods resides in the difference between the mean and median magnification of their sample.

¹³ Although the galaxies in Jolly et al. (2021) cover wider SFR and stellar mass ranges (reaching $\log(\text{SFR}/M_{\odot} \text{ yr}^{-1}) < -0.5$), a fair comparison with our sample of [CII] nondetections is still feasible if considering their high-SFR subsample which nicely matches our SFR distribution, and for which they found $\log(L_{[\text{CII}]} / L_{\odot}) < 7.7 - 7.9$, depending on the stacking method used.

¹⁴ We follow here Cassata et al. (2020), for which a $\text{Ly}\alpha$ emitter is defined as a source with rest-frame equivalent width $\text{EW}_0(\text{Ly}\alpha) > 25 \text{ \AA}$.

About this, it is interesting to note that our $L_{[\text{CII}]}$ -SFR slope (i.e., $b = 1.14 \pm 0.11$) is also consistent with that found by De Looze et al. (2014) for metal-poor dwarf galaxies in the local Universe (i.e., $b \sim 1.25$). This is in line with the results from Faisst et al. (2020) who compared the $\text{H}\alpha$ (which is a good tracer of the star-formation properties of galaxies) and [CII] luminosities for a subsample of the ALPINE galaxies. They found that bright [CII] galaxies are in good agreement with the local relation between $\text{H}\alpha$ and [CII] found by De Looze et al. (2014). However, for lower [CII] luminosities ($< 5 \times 10^8 L_{\odot}$, as those probed by the [CII] nondetections), the galaxies seem to be more consistent with the relation found for local metal-poor dwarf galaxies, although with a large scatter. The possible effect of metallicity on [CII] is also suggested by the results of Faisst et al. (2020) who noticed that the strength of [CII] emission increases along the main-sequence, with a significant decrease of [CII] content in galaxies with $\log(M_{*}/M_{\odot}) < 9.3$ and $\log(\text{SFR}/M_{\odot} \text{ yr}^{-1}) < 1$ (i.e., in [CII]-undetected sources). This further suggests that the metallicity of galaxies (along with the strength of their [CII] emission) could play an important role in the derivation of the $L_{[\text{CII}]}$ -SFR relation (Vallini et al. 2015; Olsen et al. 2017; Lagache et al. 2018; Narayanan et al. 2018; Ferrara et al. 2019). Future investigations of this topic will be possible thanks to the forthcoming near- and mid-infrared observations of the *James Webb* Space Telescope, through which we will be able to provide measurements of the metallicity content of distant galaxies.

To better understand the relation between [CII] and SFR in normal $z \sim 5$ galaxies, we compare our result with those of different simulations. Lagache et al. (2018) used the semi-analytical model G.A.S. (Galaxy Assembly from dark-matter Simulations) in combination with the photoionization code CLOUDY (Ferland et al. 2013, 2017) to predict the [CII] luminosity of a large number of galaxies at $z \sim 5$. They found an average relation with a slope in agreement with the one by De Looze et al. (2014) for HII/starburst galaxies at low redshift, but that is dependent on several parameters, such as the metallicity of the galaxies and the intensity of their interstellar radiation field. More recently, Arata et al. (2020) combined cosmological hydrodynamic simulations performed with the GADGET-3 code (Springel 2005), with the All-wavelength Radiative Transfer with Adaptive Refinement Tree (ART²) code (Li et al. 2008; Yajima et al. 2012) to predict the relation between [CII] and SFR for galaxies well within the Reionization epoch, at $z > 6$. They found a steep slope (i.e., $b = 1.47$) of the relation, suggesting that the deviation from the local Universe is caused by changes in the distribution of neutral gas in high- z galaxies. Observationally, similar results were obtained by Harikane et al. (2020) who found a very steep slope (i.e., $b = 1.6$) by analyzing a sample of $6 < z < 9$ LBGs and SMGs. They used CLOUDY to investigate the physics below their results, finding that such a slope (that is mainly caused by galaxies with low $L_{[\text{CII}]} / \text{SFR}$ ratios at low SFRs) could be produced by a high ionization parameter (as a result of a strong correlation between gas-phase metallicity and SFR, or of a bursty star formation in galaxies) and/or by a low PDR covering fraction (that is where most of the [CII] emission comes from).

Our results differ significantly from those obtained by Harikane et al. (2020) and simulated by Arata et al. (2020). As suggested by Schaerer et al. (2020), this could be due to the fact that we used a uniform estimation of the total SFR based on rest-frame UV and FIR measurements, instead of using SED-based SFRs which are typically affected by the choice of the star-formation histories, dust-attenuation curves, and

stellar populations (e.g., Carniani et al. 2020). On the other hand, Harikane et al. (2020) claimed that the difference in the method of computing SFRs does not significantly affect the estimate of the $L_{\text{[CII]}}$ -SFR relation, rather the different slope could be ascribed to a change in the properties of galaxies from $z \sim 5$ to higher redshift, or to a diverse selection of the parent sample. However, in order to put stronger constraints on the [CII] properties in the early Universe, further observations at $\log(\text{SFR}/M_{\odot}\text{yr}^{-1}) < 1$ are needed.

Finally, it is worth noting that, both in the stack and in the fit, we do not include nine nondetections having less precise spectroscopic redshifts than those from the other galaxies in the sample (see Sect. 2.2). As evidenced in Fig. 5, some of these sources show the largest deviation from the derived $L_{\text{[CII]}}$ -SFR relation, suggesting the possible presence of the so-called “[CII]-deficit” (e.g., Malhotra et al. 2001; Vallini et al. 2015; Lagache et al. 2018; Harikane et al. 2020). However, these galaxies are likely affected by a poor estimate of their spectroscopic redshifts with respect to the other ALPINE nondetections. Indeed, for the analysis undertaken in this work, an inaccurate derivation of z_{spec} could induce a not physical offset between the rest-frame UV spectroscopic redshift and the systemic one as traced by the [CII] line that we are not able to correct based on the observed $\Delta v_{\text{Ly}\alpha}$ distribution. At worst, the expected emission line could be moved outside of the ALMA spectral window of observation. In this scenario, we claim that there is no evidence of [CII]-deficit within the ALPINE sample, as also suggested by Schaerer et al. (2020).

6. Summary and conclusions

It is now well established that in the local Universe a linear relation between the [CII] luminosity and the SFR of galaxies is in place (e.g., De Looze et al. 2014). Whether this relation holds at earlier epochs is still debated. At high redshifts, the number of [CII] detections is increasing, but there are still few constraints from the low SFR, stellar mass regime, which are fundamental to properly characterize the $L_{\text{[CII]}}$ -SFR relation over cosmic time. Indeed, only a handful of low-SFR, high- z sources have been detected (or undetected) so far in [CII], most of them as strongly lensed galaxies (e.g., Knudsen et al. 2016; Carniani et al. 2017; Laporte et al. 2019; Fujimoto et al. 2021; Jolly et al. 2021; Laporte et al. 2021).

In this work, we perform a spectral stacking of 34 [CII]-undetected galaxies at $z \sim 5$, as part of the ALPINE survey, taking into account the typical observed rest-frame UV-FIR spectral offset between the Ly α and [CII] lines (Cassata et al. 2020). The stack reveals a [CII] detection at $\sim 5.1\sigma$, providing one of the few constraints on the $L_{\text{[CII]}}$ -SFR relation at high redshift and in the low-SFR regime, and resulting in a line luminosity of $\log(L_{\text{[CII]}}/L_{\odot}) \sim 7.8$. By fitting the average [CII] luminosity from the stacking of the nondetections with that from the individual ALPINE [CII]-detected galaxies as a function of their total SFRs, we find a linear relation that is comparable with the local one (1.14 ± 0.11 from this work against 1.00 ± 0.04 from De Looze et al. 2014) and in agreement with the previous results by Schaerer et al. (2020), suggesting that [CII] is still a good tracer of star formation in the early Universe. In this respect, we do not even find evidence of the so-called [CII]-deficit, that could steepen the $L_{\text{[CII]}}$ -SFR slope as found in previous works (e.g., Harikane et al. 2020).

However, further and deeper observations are needed in order to confirm these results, especially in the low SFR regime, where the $L_{\text{[CII]}}$ -SFR relation is consistent from the

spatially resolved and the entire galaxy scales, and where only a handful of strongly lensed galaxies have been detected so far at $\log(\text{SFR}/M_{\odot}\text{yr}^{-1}) \lesssim 0.5$ (e.g., Knudsen et al. 2016; Fujimoto et al. 2021). Current simulations provide different results at high redshift, suggesting that many physical mechanisms could be in place in the ISM of distant galaxies (e.g., Lagache et al. 2018; Arata et al. 2020). Further constraints, as the one provided in this work, on the low $L_{\text{[CII]}}$ and SFR tail of normal high- z SFGs could serve as input for such cosmological simulations in order to shed light on the physics of [CII] in the early Universe.

Acknowledgements. We warmly thank the anonymous referee for her/his careful reading of our paper and for the constructive comments and useful suggestions that have contributed to improve the quality of the work. This paper is based on data obtained with the ALMA Observatory, under Large Program 2017.1.00428.L. ALMA is a partnership of ESO (representing its member states), NSF(USA) and NINS (Japan), together with NRC (Canada), MOST and ASIAA (Taiwan), and KASI (Republic of Korea), in cooperation with the Republic of Chile. The Joint ALMA Observatory is operated by ESO, AUI/NRAO and NAOJ. M.R. acknowledges support from the Narodowe Centrum Nauki (UMO-2020/38/E/ST9/00077). M.T. acknowledges the support from grant PRIN MIUR 2017 20173ML3WW 001. This work was supported by the Programme National Cosmology et Galaxies (PNCG) of CNRS/INSU with INP and IN2P3, co-funded by CEA and CNES. The Cosmic Dawn Center is funded by the Danish National Research Foundation under grant No. 140. This project has received funding from the European Union’s Horizon 2020 research and innovation program under the Marie Skłodowska-Curie grant agreement No. 847523 “INTERACTIONS”. G.C.J. acknowledges ERC Advanced Grant 695671 “QUENCH” and support by the Science and Technology Facilities Council (STFC). M.B. gratefully acknowledges support by the ANID BASAL project FB210003 and from the FONDECYT regular grant 1211000. This paper is dedicated to the memory of Olivier Le Fèvre, PI of the ALPINE survey.

References

- Arata, S., Yajima, H., Nagamine, K., Abe, M., & Khochfar, S. 2020, *MNRAS*, **498**, 5541
- Bakx, T. J. L. C., Tamura, Y., Hashimoto, T., et al. 2020, *MNRAS*, **493**, 4294
- Béthermin, M., Fudamoto, Y., Ginolfi, M., et al. 2020, *A&A*, **643**, A2
- Bischoff, M., Maiolino, R., Carniani, S., et al. 2019, *A&A*, **630**, A59
- Bouwens, R. J., Smit, R., Schouws, S., et al. 2021, *ApJ*, submitted [arXiv:2106.13719]
- Brammer, G. B., van Dokkum, P. G., Franx, M., et al. 2012, *ApJS*, **200**, 13
- Capak, P. L., Carilli, C., Jones, G., et al. 2015, *Nature*, **522**, 455
- Cardamone, C. N., van Dokkum, P. G., Urry, C. M., et al. 2010, *ApJS*, **189**, 270
- Carilli, C. L., & Walter, F. 2013, *ARA&A*, **51**, 105
- Carniani, S., Maiolino, R., Pallottini, A., et al. 2017, *A&A*, **605**, A42
- Carniani, S., Maiolino, R., Smit, R., & Amorín, R. 2018a, *ApJ*, **854**, L7
- Carniani, S., Maiolino, R., Amorín, R., et al. 2018b, *MNRAS*, **478**, 1170
- Carniani, S., Ferrara, A., Maiolino, R., et al. 2020, *MNRAS*, **499**, 5136
- Carvajal, R., Bauer, F. E., Bouwens, R. J., et al. 2020, *A&A*, **633**, A160
- Cassata, P., Morselli, L., Faisst, A., et al. 2020, *A&A*, **643**, A6
- Chabrier, G. 2003, *PASP*, **115**, 763
- Cheng, C., Ibar, E., Hughes, T. M., et al. 2018, *MNRAS*, **475**, 248
- Cohen, J. 1988, *Statistical Power Analysis for the Behavioral Sciences* (Routledge)
- Cormier, D., Lebouteiller, V., Madden, S. C., et al. 2012, *A&A*, **548**, A20
- De Looze, I., Cormier, D., Lebouteiller, V., et al. 2014, *A&A*, **568**, A62
- Dessauges-Zavadsky, M., Ginolfi, M., Pozzi, F., et al. 2020, *A&A*, **643**, A5
- Dijkstra, M. 2014, *PASA*, **31**, e040
- Dunlop, J. S., McLure, R. J., Biggs, A. D., et al. 2017, *MNRAS*, **466**, 861
- Efron, B. 1982, *The Jackknife, the Bootstrap and Other Resampling Plans*
- Erb, D. K., Steidel, C. C., Shapley, A. E., Pettini, M., & Adelberger, K. L. 2004, *ApJ*, **612**, 122
- Faisst, A. L., Schaerer, D., Lemaux, B. C., et al. 2020, *ApJS*, **247**, 61
- Ferland, G. J., Porter, R. L., van Hoof, P. A. M., et al. 2013, *Rev. Mex. Astron. Astronomia*, **49**, 137
- Ferland, G. J., Chatzikos, M., Guzmán, F., et al. 2017, *Rev. Mex. Astron. Astronomia*, **53**, 385
- Ferrara, A., Vallini, L., Pallottini, A., et al. 2019, *MNRAS*, **489**, 1
- Franco, M., Elbaz, D., Béthermin, M., et al. 2018, *A&A*, **620**, A152
- Fudamoto, Y., Oesch, P. A., Faisst, A., et al. 2020, *A&A*, **643**, A4
- Fudamoto, Y., Oesch, P. A., Schouws, S., et al. 2021, *Nature*, **597**, 489

- Fujimoto, S., Ouchi, M., Ferrara, A., et al. 2019, *ApJ*, **887**, 107
- Fujimoto, S., Silverman, J. D., Bethermin, M., et al. 2020, *ApJ*, **900**, 1
- Fujimoto, S., Oguri, M., Brammer, G., et al. 2021, *ApJ*, **911**, 99
- Gallerani, S., Pallottini, A., Feruglio, C., et al. 2018, *MNRAS*, **473**, 1909
- Giavalisco, M., Ferguson, H. C., Koekemoer, A. M., et al. 2004, *ApJ*, **600**, L93
- Ginolfi, M., Jones, G. C., Béthermin, M., et al. 2020, *A&A*, **633**, A90
- Grupponi, C., Béthermin, M., Loiacono, F., et al. 2020, *A&A*, **643**, A8
- Guo, Y., Ferguson, H. C., Giavalisco, M., et al. 2013, *ApJS*, **207**, 24
- Harikane, Y., Ouchi, M., Inoue, A. K., et al. 2020, *ApJ*, **896**, 93
- Hashimoto, T., Inoue, A. K., Mawatari, K., et al. 2019, *PASJ*, **71**, 71
- Hasinger, G., Cappelluti, N., Brunner, H., et al. 2007, *ApJS*, **172**, 29
- Hasinger, G., Capak, P., Salvato, M., et al. 2018, *ApJ*, **858**, 77
- Heintz, K. E., Watson, D., Oesch, P. A., Narayanan, D., & Madden, S. C. 2021, *ApJ*, **922**, 147
- Hollenbach, D. J., & Tielens, A. G. G. M. 1999, *Rev. Mod. Phys.*, **71**, 173
- Jolly, J.-B., Knudsen, K., Laporte, N., et al. 2021, *A&A*, **652**, A128
- Jones, G. C., Vergani, D., Romano, M., et al. 2021, *MNRAS*, **507**, 3540
- Kelly, B. C. 2007, *ApJ*, **665**, 1489
- Khusanova, Y., Bethermin, M., Le Fèvre, O., et al. 2021, *A&A*, **649**, A152
- Knudsen, K. K., Richard, J., Kneib, J.-P., et al. 2016, *MNRAS*, **462**, L6
- Koekemoer, A. M., Aussel, H., Calzetti, D., et al. 2007, *ApJS*, **172**, 196
- Kohandel, M., Pallottini, A., Ferrara, A., et al. 2019, *MNRAS*, **487**, 3007
- Kroupa, P., & Weidner, C. 2003, *ApJ*, **598**, 1076
- Lagache, G., Cousin, M., & Chatzikos, M. 2018, *A&A*, **609**, A130
- Laigle, C., McCracken, H. J., Ilbert, O., et al. 2016, *ApJS*, **224**, 24
- Laporte, N., Katz, H., Ellis, R. S., et al. 2019, *MNRAS*, **487**, L81
- Laporte, N., Zitrin, A., Ellis, R. S., et al. 2021, *MNRAS*, **505**, 4838
- Le Fèvre, O., Tasca, L. A. M., Cassata, P., et al. 2015, *A&A*, **576**, A79
- Le Fèvre, O., Béthermin, M., Faisst, A., et al. 2020, *A&A*, **643**, A1
- Li, Y., Hopkins, P. F., Hernquist, L., et al. 2008, *ApJ*, **678**, 41
- Lindroos, L., Knudsen, K. K., Vlemmings, W., Conway, J., & Martí-Vidal, I. 2015, *MNRAS*, **446**, 3502
- Madau, P., & Dickinson, M. 2014, *ARA&A*, **52**, 415
- Malhotra, S., Kaufman, M. J., Hollenbach, D., et al. 2001, *ApJ*, **561**, 766
- Marchi, F., Pentericci, L., Guaita, L., et al. 2019, *A&A*, **631**, A19
- Matthee, J., Sobral, D., Boogaard, L. A., et al. 2019, *ApJ*, **881**, 124
- McCracken, H. J., Milvang-Jensen, B., Dunlop, J., et al. 2012, *A&A*, **544**, A156
- McMullin, J. P., Waters, B., Schiebel, D., Young, W., & Golap, K. 2007, in *Astronomical Data Analysis Software and Systems XVI*, eds. R. A. Shaw, F. Hill, & D. J. Bell, *ASP Conf. Ser.*, **376**, 127
- Méndez-Hernández, H., Ibar, E., Knudsen, K. K., et al. 2020, *MNRAS*, **497**, 2771
- Messa, M., Adamo, A., Östlin, G., et al. 2019, *MNRAS*, **487**, 4238
- Narayanan, D., Davé, R., Johnson, B. D., et al. 2018, *MNRAS*, **474**, 1718
- Nayyeri, H., Hemmati, S., Mobasher, B., et al. 2017, *ApJS*, **228**, 7
- Noeske, K. G., Weiner, B. J., Faber, S. M., et al. 2007, *ApJ*, **660**, L43
- Olsen, K., Greve, T. R., Narayanan, D., et al. 2017, *ApJ*, **846**, 105
- Pentericci, L., Carniani, S., Castellano, M., et al. 2016, *ApJ*, **829**, L11
- Pineda, J. L., Langer, W. D., & Goldsmith, P. F. 2014, *A&A*, **570**, A121
- Pozzi, F., Calura, F., Fudamoto, Y., et al. 2021, *A&A*, **653**, A84
- Rodighiero, G., Daddi, E., Baronchelli, I., et al. 2011, *ApJ*, **739**, L40
- Romano, M., Cassata, P., Morselli, L., et al. 2021, *A&A*, **653**, A111
- Sanders, D. B., Salvato, M., Aussel, H., et al. 2007, *ApJS*, **172**, 86
- Schaerer, D., Ginolfi, M., Béthermin, M., et al. 2020, *A&A*, **643**, A3
- Scoville, N., Abraham, R. G., Aussel, H., et al. 2007a, *ApJS*, **172**, 38
- Scoville, N., Aussel, H., Brusa, M., et al. 2007b, *ApJS*, **172**, 1
- Shao, J., & Wu, C. F. J. 1989, *Ann. Stat.*, **17**, 1176
- Skelton, R. E., Whitaker, K. E., Momcheva, I. G., et al. 2014, *ApJS*, **214**, 24
- Smit, R., Bouwens, R. J., Carniani, S., et al. 2018, *Nature*, **553**, 178
- Smolčić, V., Novak, M., Bondi, M., et al. 2017, *A&A*, **602**, A1
- Solomon, P. M., Downes, D., & Radford, S. J. E. 1992, *ApJ*, **398**, L29
- Speagle, J. S., Steinhardt, C. L., Capak, P. L., & Silverman, J. D. 2014, *ApJS*, **214**, 15
- Springel, V. 2005, *MNRAS*, **364**, 1105
- Stacey, G. J., Geis, N., Genzel, R., et al. 1991, *ApJ*, **373**, 423
- Stanley, F., Jolly, J. B., König, S., & Knudsen, K. K. 2019, *A&A*, **631**, A78
- Steidel, C. C., Erb, D. K., Shapley, A. E., et al. 2010, *ApJ*, **717**, 289
- Steidel, C. C., Bogosavljević, M., Shapley, A. E., et al. 2018, *ApJ*, **869**, 123
- Taniguchi, Y., Scoville, N., Murayama, T., et al. 2007, *ApJS*, **172**, 9
- Taniguchi, Y., Kajisawa, M., Kobayashi, M. A. R., et al. 2015, *PASJ*, **67**, 104
- Tasca, L. A. M., Le Fèvre, O., Hathi, N. P., et al. 2015, *A&A*, **581**, A54
- Tasca, L. A. M., Le Fèvre, O., Ribeiro, B., et al. 2017, *A&A*, **600**, A110
- Vallini, L., Gallerani, S., Ferrara, A., Pallottini, A., & Yue, B. 2015, *ApJ*, **813**, 36
- Vallini, L., Ferrara, A., Pallottini, A., & Gallerani, S. 2017, *MNRAS*, **467**, 1300
- Vallini, L., Ferrara, A., Pallottini, A., Carniani, S., & Gallerani, S. 2020, *MNRAS*, **495**, L22
- Verhamme, A., Orlicová, I., Schaerer, D., & Hayes, M. 2015, *A&A*, **578**, A7
- Villanueva, V., Ibar, E., Hughes, T. M., et al. 2017, *MNRAS*, **470**, 3775
- Wagg, J., Wiklind, T., Carilli, C. L., et al. 2012, *ApJ*, **752**, L30
- Wang, R., Wagg, J., Carilli, C. L., et al. 2013, *ApJ*, **773**, 44
- Wolfire, M. G., McKee, C. F., Hollenbach, D., & Tielens, A. G. G. M. 2003, *ApJ*, **587**, 278
- Yajima, H., Li, Y., Zhu, Q., & Abel, T. 2012, *MNRAS*, **424**, 884
- Zanella, A., Daddi, E., Magdis, G., et al. 2018, *MNRAS*, **481**, 1976

¹ Dipartimento di Fisica e Astronomia, Università di Padova, Vicolo dell'Osservatorio 3, 35122 Padova, Italy

e-mail: michael.romano@studenti.unipd.it

² INAF – Osservatorio Astronomico di Padova, Vicolo dell'Osservatorio 5, 35122 Padova, Italy

³ National Center for Nuclear Research, ul. Pasteura 7, 02-093 Warsaw, Poland

⁴ Associazione Big Data, Via Piero Gobetti 101, 40129 Bologna, Italy

⁵ European Southern Observatory, Karl-Schwarzschild-Strasse 2, 85748 Garching, Germany

⁶ Observatoire de Genève, Université de Genève, 51 Ch. des Maillettes, 1290 Versoix, Switzerland

⁷ Aix Marseille Univ, CNRS, CNES, LAM, Marseille, France

⁸ Infrared Processing and Analysis Center, California Institute of Technology, Pasadena, CA 91125, USA

⁹ IPAC, California Institute of Technology, 1200 East California Boulevard, Pasadena, CA 91125, USA

¹⁰ Kavli Institute for the Physics and Mathematics of the Universe, The University of Tokyo Kashiwa, Chiba 277-8583, Japan

¹¹ Department of Astronomy, School of Science, The University of Tokyo, 7-3-1 Hongo, Bunkyo, Tokyo 113-0033, Japan

¹² The Caltech Optical Observatories, California Institute of Technology, Pasadena, CA 91125, USA

¹³ INAF – Osservatorio di Astrofisica e Scienza dello Spazio, Via Gobetti 93/3, 40129 Bologna, Italy

¹⁴ Centro de Astronomía (CITEVA), Universidad de Antofagasta, Avenida Angamos 601, Antofagasta, Chile

¹⁵ Cosmic Dawn Center (DAWN), Jagtvej 128, 22000 Copenhagen N, Denmark

¹⁶ Niels Bohr Institute, University of Copenhagen, Lyngbyvej 2, 2100 Copenhagen Ø, Denmark

¹⁷ Space Telescope Science Institute, 3700 San Martin Drive, Baltimore, MD 21218, USA

¹⁸ Cavendish Laboratory, University of Cambridge, 19 J. J. Thomson Ave., Cambridge CB3 0HE, UK

¹⁹ Kavli Institute for Cosmology, University of Cambridge, Madingley Road, Cambridge CB3 0HA, UK

²⁰ Department of Physics and Astronomy, University of California, Davis, One Shields Ave., Davis, CA 95616, USA

²¹ Gemini Observatory, NSF's NOIRLab, 670 N. A'ohoku Place, Hilo, Hawai'i 96720, USA

²² Instituto de Física y Astronomía, Universidad de Valparaíso, Avda. Gran Bretaña 1111, 2340000 Valparaíso, Chile

²³ Department of Astronomy, University of Florida, 211 Bryant Space Sciences Center, Gainesville 32611, USA

²⁴ University of Florida Informatics Institute, 432 Newell Drive, CISE Bldg E251, Gainesville 32611, USA

²⁵ Cosmic Dawn Center at the Niels Bohr Institute, University of Copenhagen and DTU-Space, Technical University of Denmark, Denmark

²⁶ University of Bologna – Department of Physics and Astronomy “Augusto Righi” (DIFA), Via Gobetti 93/2, 40129 Bologna, Italy